

## Intraband terahertz emission from coupled semiconductor quantum wells: A model study using the exciton representation

Wei Min Zhang, Torsten Meier,\* Vladimir Chernyak, and Shaul Mukamel

*Department of Chemistry and Rochester Theory Center for Optical Science and Engineering, University of Rochester,  
Rochester, New York 14627*

(Received 2 September 1998; revised manuscript received 12 January 1999)

Intraband emission resulting from the second-order polarization induced by a femtosecond pump field in semiconductor nanostructures is calculated. The two-band model is transformed to the exciton representation, and exciton-phonon coupling represented by arbitrary spectral densities is incorporated into the equations of motion for the relevant exciton variables through Redfield superoperators. Time-resolved coherent and incoherent terahertz radiation as well as the incoherent optical fluorescence are calculated for a one-dimensional model of coupled quantum wells in an external electric field with on-site Coulomb interaction between electrons and holes and an overdamped Brownian oscillator spectral density representing the electron-phonon coupling. A doorway-window picture based on the reduced single-electron density matrix is developed for the analysis of both signals. Disorder and phonon-induced dephasing effects on the various signals are discussed and compared. [S0163-1829(99)00724-9]

### I. INTRODUCTION

A novel technique known as terahertz (THz) spectroscopy has been applied recently to various semiconductor nanostructures including semiconductor surfaces,<sup>1,2</sup> single<sup>3</sup> and double quantum wells,<sup>4</sup> as well as superlattices.<sup>5</sup> In this spectroscopy the emitted electric field originating from intraband motion of optically excited carriers is detected. The relevant transition energies, as well as the spectral widths of the exciting laser pulses are typically on the order of a few up to tens meV and correspondingly the emitted radiation is in the THz range.

A number of microscopic calculations of these THz signals have been performed,<sup>6-8</sup> based on the semiconductor Bloch equations (SBE) (Refs. 9,10) and its extensions for multisubband systems.<sup>6,8,11</sup> Since these models include the Coulomb interaction within the time-dependent Hartree-Fock approximation, they describe the effects of bound excitons as well as the correlated electron-hole scattering continuum (for a recent theoretical approach that describes nonlinear optical processes in metals and doped quantum wells see Ref. 12). Dephasing due to carrier-phonon interactions have been included as well.<sup>8,13,14</sup> Typically this is done using Boltzmann-like equations for the interband-polarization and the populations<sup>14-16</sup> in which the relaxation kernel is calculated to second order in the electron-phonon coupling, and the Markov approximation is employed. Carrier-carrier scattering, which is a second-order process induced by Coulomb interaction and which becomes important at high excitation densities can be treated similarly.<sup>13-15,17,18</sup>

In a recent discussion of intracollisional field effect,<sup>19</sup> it has been demonstrated that when the carrier-phonon interaction is calculated approximately (especially using the Markov approximation) the result in general may depend on the chosen basis. In Ref. 16 it has been shown that in semiconductor superlattices one gets different damping rates of the THz signal, when the carrier-LO-phonon scattering rates are

calculated in a plane-wave representation using a field-independent basis set, compared to the Wannier-Stark representation, where the applied field is included in the basis. Since the latter representation includes more interactions, the results should, especially for high applied fields, be more realistic. To obtain similar results within the plane-wave representation one would have to perform time-consuming non-Markovian calculations. It is therefore clear that one should include as many interactions as possible in the basis set used to evaluate the electron-phonon coupling. Here we go one step further compared to Ref. 16 and also include the Coulomb interaction (and disorder, if present,) in the basis set. In a description of linear optical properties of superlattices using a three-dimensional model, an exciton basis set has been employed by Dignam and Sipe.<sup>20</sup> Later Dignam *et al.*<sup>21</sup> used this approach to investigate the coherent THz emission from superlattices. These calculations included, however, no microscopic description of dephasing processes.

It has been shown in a large number of publications that dephasing strongly affects the coherent THz transients.<sup>6,7,14,22-27</sup> Since a description of dephasing typically makes use of certain approximations which may give different results when analyzed in different basis sets, one should use the most adequate basis. Here we use a basis set which fully includes all purely electronic terms in the Hamiltonian.

In this paper we calculate the intraband emission arising from a few coupled semiconductor quantum wells to lowest order in the optical fields, i.e., treating it as a  $\chi^{(2)}$  process. To keep the numerical effort manageable we restrict our description to a one-dimensional model of coupled quantum wells, where the motion in the plane of the quantum wells is ignored. We first transform our Hamiltonian into the exciton basis. All purely electronic terms appearing in the Hamiltonian, the coupling between the quantum wells, the applied field, the Coulomb interaction, as well as energetic disorder (if present), are included in the basis set. This exciton basis is used to describe the coupling to phonons, which is evaluated

via relaxation superoperators calculated perturbatively in the exciton-phonon coupling. That coupling is incorporated in the Hamiltonian through spectral densities using the multi-mode Brownian oscillator model.<sup>28</sup> We then calculate the coherent and incoherent THz transients originating from intraband emission using the overdamped Brownian oscillator model. For comparison, the optical fluorescence signal which is related to interband transitions is discussed as well. Two equivalent but complementary physical pictures are applied for analyzing the signals. First, the numerical results are interpreted directly using the exciton basis set, which has been used in the calculations. In addition, the real-space electron and hole populations which are responsible for the coherent emission, and the density matrices are calculated by a transformation from the exciton space. These pictures are both applied towards the interpretation and explanation of the origin of the modulations appearing in the coherent THz signal for short times, as well as for the long time relaxation, which eventually for strong applied fields leads to charge separation between the optically excited electrons and holes.

In Sec. II we present the Hamiltonian and details of the exciton representation and the electron-phonon coupling. Expressions for the intraband polarizations and the equations of motion for exciton polarizations, populations and coherences are presented in Sec. III. Expressions for the relaxation superoperator are derived in Appendix A. In Sec. IV we present the formalism of the interband polarization and optical fluorescence. Numerical results are given in Sec. V and we close in Sec. VI with a brief discussion.

## II. THE NONLINEAR EXCITON EQUATIONS (NEE) FOR THE TWO-BAND MODEL

We start with the two-band model Hamiltonian for one-dimensional coupled semiconductor quantum wells

$$H = H_0 + H_c + H_{\text{ph}} + H_{\text{int}}, \quad (2.1)$$

where  $H_0$  describes the free electrons and holes

$$H_0 = \sum_{mn} E_{mn}^e c_m^\dagger c_n + \sum_{mn} E_{mn}^h d_m^\dagger d_n. \quad (2.2)$$

Here,  $c_m^\dagger(d_m^\dagger)$  creates and  $c_m(d_m)$  annihilates an electron (a hole) in the  $m$ th quantum well.  $H_c$  represents the Coulomb interactions

$$H_c = \sum_{m n k l} \left( \frac{1}{2} V_{m n k l}^e c_m^\dagger c_n^\dagger c_k c_l + \frac{1}{2} V_{m n k l}^h d_m^\dagger d_n^\dagger d_k d_l - V_{m n k l} c_m^\dagger d_n^\dagger d_k c_l \right), \quad (2.3)$$

where the tetradic matrices  $V^e, V^h$ , and  $V$  denote electron-electron, hole-hole, and electron-hole Coulomb interactions, respectively, which may be different due to different confinement wave functions for electrons and holes.<sup>6,8,11</sup>  $H_{\text{ph}}$  is the phonon Hamiltonian representing a set of oscillators<sup>28</sup>

$$H_{\text{ph}} = \sum_s \left( \frac{p_s^2}{2m_s} + \frac{m_s \omega_s^2 q_s^2}{2} \right), \quad (2.4)$$

where  $s$  labels the nuclear (phonon) modes with frequency  $\omega_s$ .  $H_{\text{int}}$  represents intraband electron-phonon coupling which is assumed to be linear in the phonon coordinates

$$H_{\text{int}} = \sum_{mnj} m_s \omega_s^2 q_s (z_{mn,s}^e c_m^\dagger c_n + z_{mn,s}^h d_m^\dagger d_n). \quad (2.5)$$

The matrix elements  $z_{mn,s}^e$  and  $z_{mn,s}^h$  determine the coupling strength of the  $s$ th bath oscillator to  $c_m^\dagger c_n$  and  $d_m^\dagger d_n$ .<sup>28,29</sup> The total Hamiltonian representing the quantum wells coupled to an external electric field  $E(t)$  is

$$H_T = H - P \cdot E(t), \quad (2.6)$$

where the polarization operator contains both interband ( $P^{eh}$ ) and intraband ( $P^{ee}$  and  $P^{hh}$ ) contributions<sup>6,7,16</sup>

$$P \equiv P^{eh} + P^{ee} + P^{hh}, \quad (2.7)$$

with

$$P^{eh} = \sum_{mn} M_{mn}^{eh} (c_m^\dagger d_n^\dagger + d_n c_m), \quad (2.8)$$

$$P^{ee} = \sum_{mn} M_{mn}^{ee} c_m^\dagger c_n, \quad P^{hh} = \sum_{mn} M_{mn}^{hh} d_m^\dagger d_n, \quad (2.9)$$

where  $M_{mn}^{eh}$ ,  $M_{mn}^{ee}$ , and  $M_{mn}^{hh}$  are transition dipoles.

The optical response of this system may be calculated by introducing exciton operators  $B_\alpha$ ,  $B_\alpha^\dagger$  defined by<sup>30</sup>

$$B_\alpha^\dagger \equiv \sum_{mn} \Psi_{mn,\alpha} c_m^\dagger d_n^\dagger, \quad (2.10)$$

where the exciton wave functions  $\Psi_{mn,\alpha}$  and energies  $\epsilon_\alpha$  satisfy the eigenvalue equations

$$\sum_{n'm'} (E_{mm'}^e \delta_{nn'} + \delta_{mm'} E_{nn'}^h - V_{mnn'm'}) \Psi_{m'n',\alpha} = \epsilon_\alpha \Psi_{m'n',\alpha}. \quad (2.11)$$

The eigenstates of the electronic Hamiltonian  $H_0 + H_c$  consist of well-separated manifolds of  $n$ -exciton states,  $n = 1, 2, \dots$ . The  $\chi^{(2)}$  signals considered in the present work only depend on the one-exciton states. Using the exciton operators, these states can be represented by the Hamiltonian

$$H = \sum_\alpha \epsilon_\alpha B_\alpha^\dagger B_\alpha + H_{\text{ph}} + H_{\text{int}}, \quad (2.12)$$

with Bose commutation relations (which holds for processes up to second order in the applied field)

$$[B_\alpha, B_\beta^\dagger] = \delta_{\alpha\beta}. \quad (2.13)$$

In this representation the exciton-phonon interaction adopts the form

$$H_{\text{int}} = \sum_{\alpha\beta s} \mathcal{D}_{\alpha\beta,s} m_s \omega_s^2 B_{\alpha}^{\dagger} B_{\beta} q_s, \quad (2.14)$$

with the exciton-phonon coupling constants

$$\mathcal{D}_{\alpha\beta,s} = \sum_{mm'n'} (z_{mm',s}^e \delta_{nn'} + \delta_{mm'} z_{nn',s}^h) \Psi_{mn,\alpha}^* \Psi_{m'n',\beta}. \quad (2.15)$$

The polarization operator is given by

$$P = P_a + P_b, \quad (2.16)$$

$P_a$  and  $P_b$  represent the interband and intraband contributions, respectively,

$$P_a = \sum_{\alpha} (M_{\alpha}^a B_{\alpha} + M_{\alpha}^{a*} B_{\alpha}^{\dagger}), \quad (2.17)$$

$$P_b = \sum_{\alpha\beta} M_{\alpha\beta}^b B_{\alpha}^{\dagger} B_{\beta}, \quad (2.18)$$

where the corresponding dipole matrix elements are given by

$$M_{\alpha}^a = \sum_{mn} \Psi_{mn,\alpha} M_{mn}^{eh}, \quad (2.19)$$

$$M_{\alpha\beta}^b = \sum_{mm'n'} (M_{mm'}^{ee} \delta_{nn'} + \delta_{mm'} M_{nn'}^{hh}) \Psi_{mn,\alpha}^* \Psi_{m'n',\beta}. \quad (2.20)$$

The nonlinear exciton equations (NEE) where the response function is calculated to the third order, were derived in Ref. 29. In the present calculation, we need to consider the radiation field only up to second order, so we only have to keep the variables  $\langle B \rangle$  and  $N \equiv \langle B^{\dagger} B \rangle$ . The NEE thus become

$$i \frac{d\langle B_{\mu} \rangle}{dt} - \sum_{\nu} h_{\mu\nu}^{(1)} \langle B_{\nu} \rangle = -M_{\mu}^a E(t), \quad (2.21)$$

$$\begin{aligned} i \frac{dN_{\mu\nu}}{dt} - \sum_{\alpha\beta} h_{\mu\nu,\alpha\beta}^{(2)} N_{\alpha\beta} \\ = -M_{\nu}^a E(t) \langle B_{\mu} \rangle^* + M_{\mu}^{a*} E^*(t) \langle B_{\nu} \rangle, \end{aligned} \quad (2.22)$$

where

$$h_{\mu\nu}^{(1)} \equiv \delta_{\mu\nu} \epsilon_{\mu} - i\Gamma_{\mu\nu}, \quad (2.23)$$

$$h_{\mu\nu,\alpha\beta}^{(2)} \equiv \delta_{\mu\alpha} \delta_{\nu\beta} (\epsilon_{\nu} - \epsilon_{\mu}) - iR_{\mu\nu,\alpha\beta}. \quad (2.24)$$

Equations (2.21) and (2.22) are identical to Eqs. (2.25) and (2.27) of Ref. 29, except that they use the exciton basis set. Since the exciton basis set is obtained by a linear transformation of the real space basis, they have the same form. Exciton-phonon coupling has been incorporated in these equations through the relaxation operators  $\Gamma_{\mu\nu}$  and  $R_{\mu\nu,\alpha\beta}$  representing the dephasing matrix and the Redfield tensor, respectively. These operators may be defined formally and calculated using projection operator techniques (see Appendix A).

### III. THE TIME-RESOLVED COHERENT TERAHERTZ SIGNAL

To present the formal expressions for the signals we introduce the following notation: for any operator  $Q$  we define the Heisenberg operators  $\tilde{Q}(t)$  whose time evolution is determined by the Hamiltonians  $H_T(t)$ . In the expression for  $H_T(t)$  [Eq. (2.6)], we set  $P = P_a$ , i.e., we neglect intraband polarization in the coupling to the driving field, while keeping it in the signals. This is justified within the rotating wave approximation, since in semiconductor nanostructures the relevant intraband energy differences are typically much smaller than the band-gap energy.

The coherent Terahertz signal, representing the emission of many quantum wells, is determined by the intraband dipole moment  $\langle \tilde{P}_b(t) \rangle$ .<sup>6,7,16</sup> The first derivative of  $\langle \tilde{P}_b(t) \rangle$  with respect to time is proportional to the current

$$j_{\text{THz}}^c(t) \propto \frac{\partial}{\partial t} \langle \tilde{P}_b(t) \rangle. \quad (3.1)$$

The experiment is performed by measuring an electric field using small photoconductive dipole antennas. The far field of the emitted radiation is proportional to the second derivative of this dipole moment (like for the Hertzian oscillating dipole)<sup>6,16,31</sup>

$$E_{\text{THz}}^c(t) \propto \frac{\partial^2}{\partial t^2} \langle \tilde{P}_b(t) \rangle. \quad (3.2)$$

Hereafter, we will refer to  $\langle \tilde{P}_b(t) \rangle$  as the coherent signal, which is given by

$$\langle \tilde{P}_b(t) \rangle \equiv \text{Tr}[P_b \rho(t)], \quad (3.3)$$

with  $\rho(t) = N_{\alpha\beta}(t) \equiv \langle B_{\alpha}^{\dagger}(t) B_{\beta}(t) \rangle$  is calculated by solving Eqs. (2.21) and (2.22) with the initial conditions  $\langle B_{\mu} \rangle = N_{\mu\nu} = 0$  at  $t \rightarrow -\infty$ .  $\langle \tilde{P}_b(t) \rangle$  can be expressed in a physically transparent form by recasting it as an overlap of a doorway wavepacket representing the exciton density matrix prepared by the pump field and a window, given by the intraband dipole Eq. (2.18). We then obtain

$$\langle \tilde{P}_b(t) \rangle = \sum_{\alpha\beta} M_{\alpha\beta}^b N_{\alpha\beta}(t). \quad (3.4)$$

### IV. THE INCOHERENT TERAHERTZ AND OPTICAL FLUORESCENCE SIGNALS

We have calculated three types of optical signals. The first is the coherent emission calculated in Sec. III. The second is the incoherent THz signal which can be obtained using a straightforward generalization of a doorway-window representation developed in Ref. 32 for four-wave mixing spectroscopy. The third is the time- and frequency-resolved fluorescence.<sup>33</sup> The difference between these three types of signals is that in the case of incoherent THz signal one-exciton coherences propagate during the last time interval. For four-wave mixing spectroscopy we have the propagation of the same coherences as well as the coherences between one- and two-exciton states, see, for example, Ref. 34. The propagation of coherences between one-exciton states during

the last time interval is described by the Green function  $G_{\mu\nu,\alpha\beta}^{(2)}(t)$  of Eq. (2.22) at zero optical field  $E(t)=0$ , defined by

$$N_{\mu\nu}(t) = \sum_{\alpha\beta} G_{\mu\nu,\alpha\beta}^{(2)}(t) N_{\alpha\beta}(0). \quad (4.1)$$

The doorway-window representation for the incoherent THz signal is obtained by applying the formalism of Ref. 32 which involves the Green function  $G^{(2)}$  in the expression for the window function. This yields

$$S^{(i)}(\omega, t) = \text{Re} \sum_{\alpha\beta} W_{\alpha\beta}^{(i)}(\omega) N_{\alpha\beta}(t), \quad (4.2)$$

with the window function

$$W_{\alpha\beta}^{(i)}(\omega) \equiv 2 \sum_{\mu\nu\lambda} M_{\mu\nu}^b M_{\lambda\beta}^b \int_0^\infty dt' \exp(i\omega t') G_{\mu\nu,\alpha\lambda}^{(2)}(t'). \quad (4.3)$$

The time-resolved interband (optical) fluorescence signal

$$S_{fi}(t) \equiv \langle \tilde{P}_a^*(t) \tilde{P}_a(t) \rangle, \quad (4.4)$$

can be calculated by using the same doorway function  $N_{\alpha\beta}(t)$  as in Eq. (3.4), and a different window

$$S_{fi}(t) = \sum_{\alpha\beta} M_{\alpha}^{a*} M_{\beta}^a N_{\alpha\beta}(t), \quad (4.5)$$

which is determined by the interband dipoles.

## V. NUMERICAL RESULTS

In the following numerical calculations we study a system made out of a few ( $N=2,3,4,5$ ) coupled quantum wells in one dimension: the indices  $m=1,2,3,\dots,N$  label the quantum wells. Electronic coupling between quantum wells is included via nearest-neighbor coupling of the electron and hole levels with

$$\begin{aligned} E_{n,n+1}^e &= E_{n+1,n}^e = 2.25 \text{ meV}, \\ E_{n,n+1}^h &= E_{n+1,n}^h = 0.25 \text{ meV}. \end{aligned} \quad (5.1)$$

The coupling of the holes is assumed to be weaker than that for the electrons, reflecting the much larger effective mass of holes in III-V semiconductors. These parameters correspond to rather weakly coupled quantum wells. In the limit of infinitely many coupled quantum wells, i.e., a superlattice, the combined electron plus hole miniband-width for this nearest neighbor coupling is  $\Delta = 4(E_{n,n+1}^e + E_{n,n+1}^h) = 10 \text{ meV}$ .

The static applied fields ( $F$ ) and diagonal energetic disorder, when included, show up in the electron and hole energies

$$E_{n,n}^e = E^e - neFd + \sigma_n^e, \quad (5.2)$$

$$E_{n,n}^h = E^h + neFd + \frac{E_{n,n+1}^h}{E_{n,n+1}^e} \sigma_n^e. \quad (5.3)$$

Here  $e$  is the electron charge, and  $d$  is the periodicity length of the coupled quantum well structure, i.e., the barrier plus

the well width.  $E^e + E^h$  defines the optical transition frequency in a single quantum well neglecting the Coulomb interaction and the disorder. In the optical spectra shown later, we set  $E^e + E^h = 0$  since the absolute magnitude of the band gap is irrelevant here. To include diagonal disorder we chose  $\sigma_n^e$  from a Gaussian distribution with a width of 1.18 meV [full width at half maximum (FWHM)], and assume that the disorder for electrons and holes is correlated, which is reasonable when they both originate from well width fluctuations. The disorder in the valence band is assumed to be weaker than that in the conduction band, with a ratio determined by their coupling strength [see Eq. (5.3)].

For the Coulomb-interaction we use an on-site electron-hole Coulomb attraction model (electron-electron and hole-hole Coulomb-interaction does not affect  $\chi^{(2)}$ )

$$V_{mnlk} = \delta_{mn} \delta_{kl} \delta_{nk} V, \quad (5.4)$$

with  $V=9 \text{ meV}$ , which is a typical exciton binding energy in a GaAs quantum well. Such a Coulomb interaction together with a tight-binding model have been used previously in the description of the ultrafast response of superlattices.<sup>23-25</sup> This model was successfully applied to determine field-induced exciton ionization times from four-wave-mixing experiments.<sup>35</sup>

The coupling of electrons (holes) to the phonons is assumed diagonal in the quantum-well index:

$$z_{mn,s}^e = \delta_{mn} z_{m,s}^e, \quad z_{mn,s}^h = \delta_{mn} z_{m,s}^h. \quad (5.5)$$

We further assume  $z^e = z^h$  so that the electron-electron, hole-hole, and electron-hole spectral densities are the same. For simplicity we use a single overdamped Brownian oscillator spectral density per quantum well

$$C_{mn,kl}^{ij}(\omega) = \delta_{mn} \delta_{kl} \delta_{mk} 2\lambda \frac{\omega\tau}{\omega^2\tau^2 + 1}, \quad (5.6)$$

where  $i,j$  assumes the values  $e$  and  $h$ . This spectral density represents low frequency vibrations, i.e., acoustic phonons. In our calculation we have used the values  $\lambda = 0.1 \text{ meV}$  and  $\tau = 50 \text{ fs}$ .

### A. Optical absorption and fluorescence

The optical transition dipoles are assumed to be diagonal in the quantum-well index

$$M_{mn}^{eh} = \delta_{mn} M^{eh}. \quad (5.7)$$

Substituting Eq. (5.7) into Eq. (2.19), we obtain the exciton space interband dipole  $M_{\alpha}^a$ . Optical absorption can then be calculated by assuming a Lorentzian line shape

$$S_a(\omega) = -\text{Im} \sum_{\alpha} \frac{|M_{\alpha}^a|^2}{\omega - \omega_{\alpha} + i/T_2}. \quad (5.8)$$

Figure 1 displays the linear optical absorption spectra versus the applied field for different number of coupled quantum wells (a)  $N=2$ , (b)  $N=3$ , (c)  $N=4$ , and (d)  $N=5$ , using  $T_2 = 1 \text{ ps}$ . Note that the zero of the frequency scale corre-

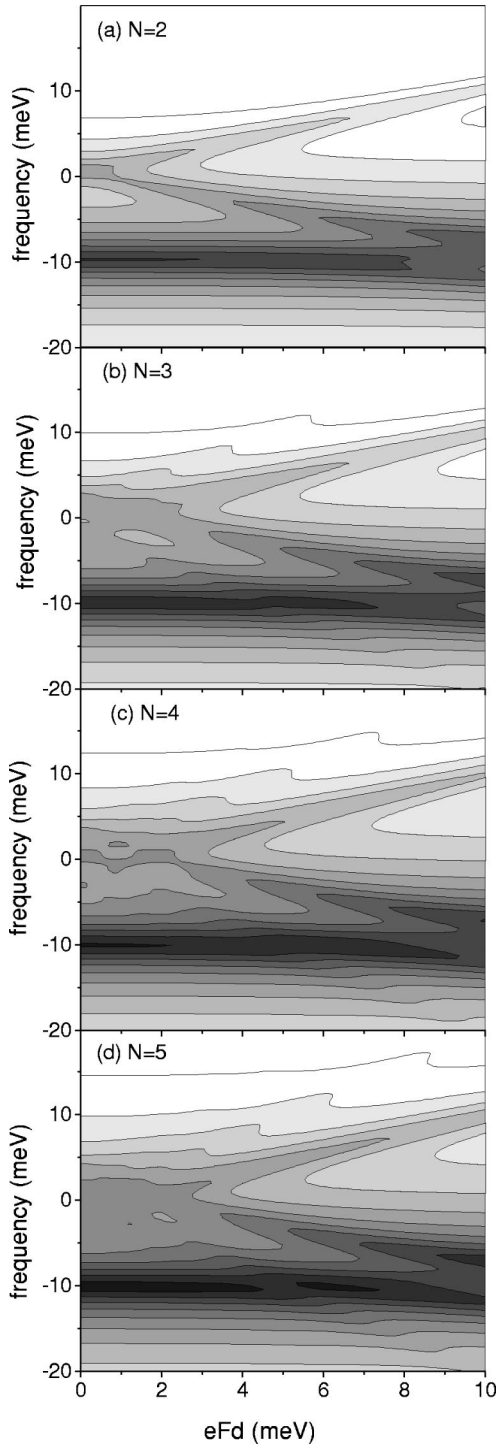


FIG. 1. Linear absorption spectra (log scale) as function of applied field (in units of  $eFd$ ). The zero of the energy scale corresponds to a single quantum well transition without Coulomb interaction. (a)  $N=2$ , (b)  $N=3$ , (c)  $N=4$ , and (d)  $N=5$ . Here coupling to phonons was not included and we have instead chosen a dephasing time of  $T_2=1$  ps for the interband polarization.

sponds to the frequency of the electron-hole transition for a single quantum well, neglecting exciton effects. One sees that in the absence of an applied field, most of the oscillator strength is concentrated in the optically active exciton, situated at about  $-10$  meV. Within the one-dimensional model, the absorption of other energetically higher transitions that can be seen around  $0$  meV, which for a superlattice would

correspond to the miniband absorption, is very weak. The absorption changes with the applied field. For a very strong field, the excitonic absorption shifts to the frequency of the single-quantum well transition minus the quantum well exciton binding energy ( $V$ ), which for our parameters gives  $-9$  meV. For the parameters used here it is very close to the position of the exciton without applied field as is typical for weakly coupled quantum wells and superlattices. Therefore over the whole range of fields displayed in Fig. 1, most of the oscillator strength is concentrated in this energy region.<sup>23</sup> New features appear with the applied field which shifts the energies of indirect optical transitions. For fields where those transitions are resonant with the exciton, their coupling leads to anticrossings, which have been observed in coupled quantum wells<sup>4</sup> and superlattices.<sup>36</sup> For  $N=2$  there is an anticrossing around  $eFd=9$  meV, for  $N=3, 4$ , and  $5$  a second anticrossing around  $eFd=5$  meV can be seen in Fig. 1.

Within the one-dimensional model with  $N$  coupled quantum wells, there are  $N^2$  single excitons and consequently  $N^2$  interband polarizations related to these excitons ( $B_\mu$ ). Therefore there are  $N^4$  exciton populations and coherences ( $N_{\mu\nu}$ ). The Redfield tensor  $R$  thus has  $N^8$  components. The calculation of this Redfield tensor is the most numerically expensive step in the applications presented below.

We have computed the time-resolved optical signals by numerically solving the equations of motion Eqs. (2.21) and (2.22) for  $N=2$  and  $eFd=10$  meV. In all calculations we have tuned the central laser frequency to  $-15$  meV, corresponding to an excitation about  $5$  meV below the field-free position of the strongly absorbing exciton using Gaussian pulses with  $118$  fs (FWHM) for the laser pulse intensity, which is proportional to  $|E(t)|^2$ . Figure 2 displays the absolute square of the linear optical polarization  $|S_a(t)|^2$  and the optical fluorescence. The linear optical polarization in the time domain is given by

$$S_a(t) = \sum_{\alpha} M_{\alpha}^a \langle B_{\alpha} \rangle, \quad (5.9)$$

and the fluorescence has been calculated using Eq. (4.5). In the absence of dephasing due to coupling with phonons (the coherent limit) [Fig. 2(a)], both signals are equal. This is due to the fact, that in this case the population and coherence exciton density matrix  $N_{\alpha\beta}$  can be expressed via the interband amplitudes<sup>25,28</sup>  $\langle B_{\alpha} \rangle$  by

$$N_{\alpha\beta} = \langle B_{\alpha}^* \rangle \langle B_{\beta} \rangle. \quad (5.10)$$

Using this identity it is easy to show that both signals displayed in Fig. 2(a) are equal. The modulations reflect energy spacings between optically excited states. Including coupling to phonons [Fig. 2(b)] leads to a rapid decay of the optical polarization, whereas the damping of the fluorescence is considerably slower. Due to the phonon-induced relaxation, coherences between excited states, which are responsible for the modulations of the fluorescence are rapidly damped. We notice a somewhat different oscillation pattern in Fig. 2(b) compared to Fig. 2(a). This is due to the fact that phonons coupled via the Redfield relaxation tensor shift the exciton energies. The new modulations are determined by the energy differences of phonon-dressed excitons, which can be ob-

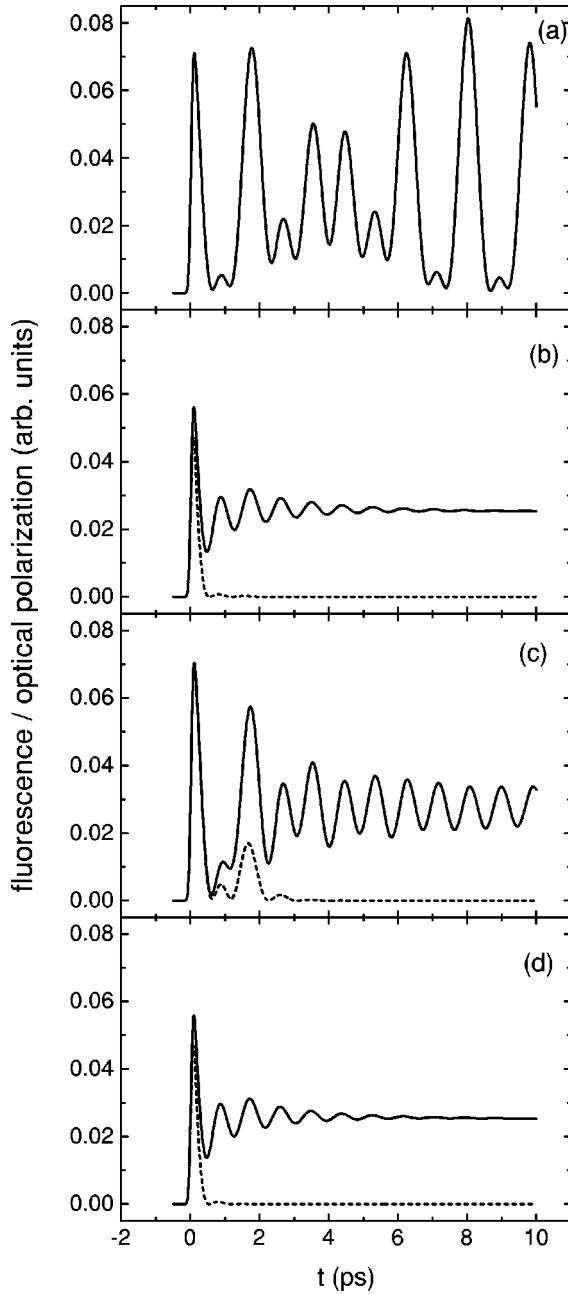


FIG. 2. Absolute square of optical polarization (dashed line) and time-resolved fluorescence (solid line). (a) without disorder and phonons, (b) Without disorder, including phonons (300 K), (c) with disorder, without phonons, (d) with both disorder and phonons (300 K).  $N=2, eFd=10$  meV.

tained as the eigenstates of the equation of motions of the populations and coherences including the relaxation tensor. Since we have not included radiative damping,<sup>37</sup> the fluorescence attains at long times a finite constant value. Averaging over disorder realizations [Fig. 2(c)] has similar effects and also induces a damping of the THz signal.<sup>22,27</sup> The optical polarization decays rapidly, since the disorder induces inhomogeneous broadening, and the modulations of fluorescence are damped as well. For the present parameters the disorder is weak, which means that the disorder fluctuations are much smaller than the energy differences between the exciton states, and their effects are rather weak.<sup>38</sup> The modulation pattern of the fluorescence is close to the one shown in Fig.

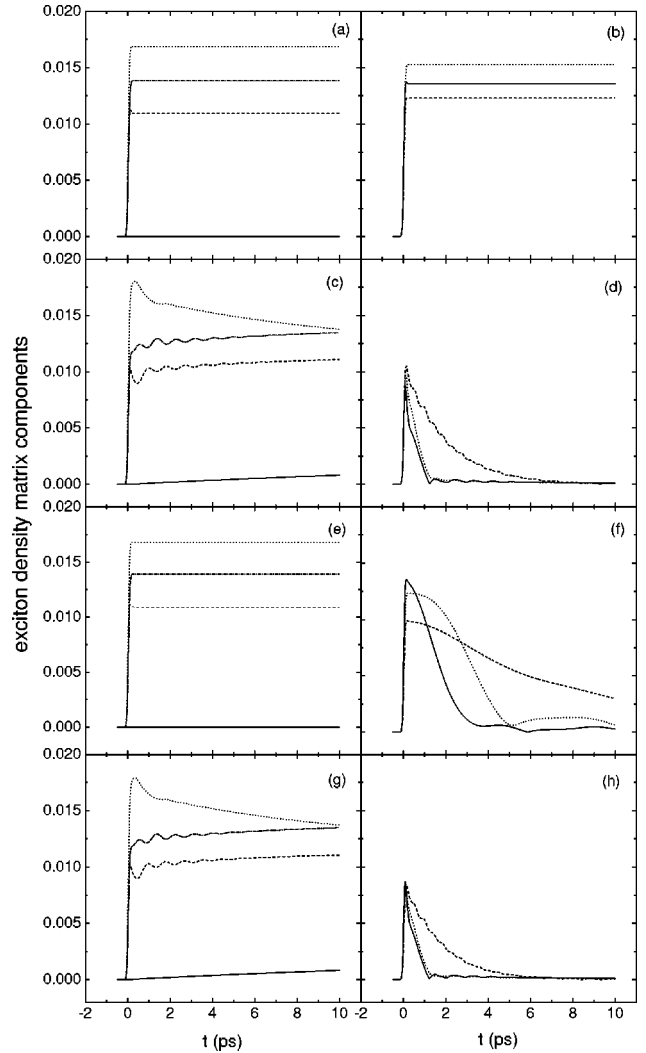


FIG. 3. Exciton density matrix for  $N=2, eFd=10$  meV. Left column, exciton populations, solid line:  $N_{11}$ , dashed line:  $N_{22}$ , dotted line:  $N_{33}$  and dash-dotted line:  $N_{44}$ . Right column, exciton coherences, solid line:  $N_{23}$ , dashed line:  $N_{24}$ , dotted line:  $N_{34}$ . (a) and (b), no phonons, no disorder; (c) and (d), phonons only; (e) and (f), disorder only; (g) and (h), both phonons and disorder.

2(a). Therefore the combined action of coupling to phonons and disorder [Fig. 2(d)] is very close to the result of the phonons alone [Fig. 2(b)]. Figure 2 shows an overall rapid decay of the interband (optical) polarization, and a slower decay of modulations of the intraband coherences.

As shown above, the incoherent fluorescence signal probes the doorway function, namely, the exciton population and coherence density matrix  $N_{\alpha\beta}$ . Figure 3 displays the exciton density matrix for various situations using the parameters of Fig. 2. We label the four ( $N^2$ ) excitons with 1, 2, 3, and 4, where exciton 1 has the highest energy and 4 the lowest. Figure 3(a) shows the populations in the absence of phonons and disorder. Figure 3(b) displays the coherence  $N_{23}$ ,  $N_{24}$ , and  $N_{34}$ . The coherences between exciton 1 with the other three excitons are very small and therefore not shown. Without phonon and disorder, they are all constant after the excitation. Including the phonons, the populations start to relax and approach an equilibrium in the long time limit (which is not reached in our finite time calculations

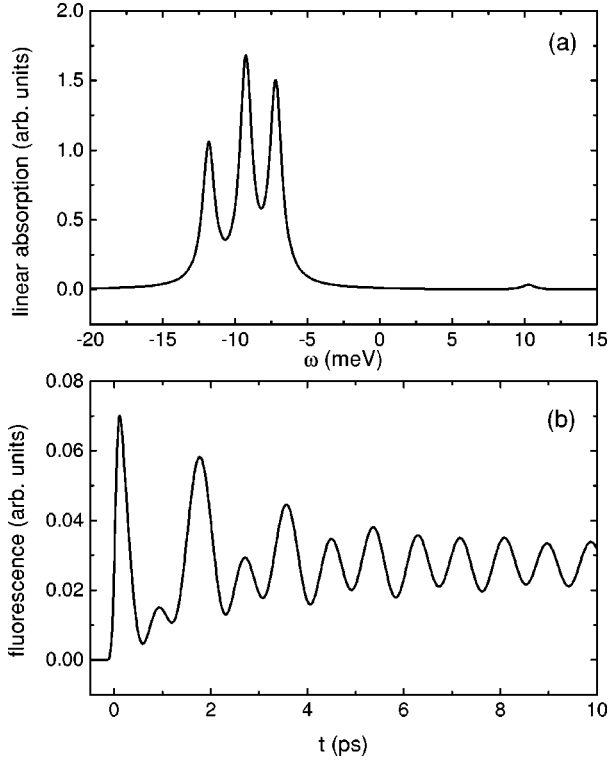


FIG. 4. Absorption (a) and optical fluorescence (b) for  $N=2$ ,  $eFd=10$  meV,  $T=50$  K.

[Fig. 3(c)], while the coherences decay to zero [Fig. 3(d)]. Figures 3(e) and 3(f) are for disorder only, where the populations remain constant, while the coherences decay slowly. The combined dynamics induced by both phonons and disorder are displayed in Figs. 3(g) and 3(h).

On a longer time scale the exciton-phonon coupling induces energy relaxation of exciton populations. In the long-time limit the system will reach an equilibrium in the space of phonon-dressed excitons. For not too strong exciton phonon coupling and at low temperatures, eventually the low energy excitons will be populated. For not too weak fields these are indirect excitons with electrons and holes at different ends of the coupled quantum well structure. Although the time scale associated with this equilibration is much longer than the times considered in our time-domain solution, the tendency towards relaxation-induced charge separation accompanying the energy relaxation for long times can be seen in Fig. 3(c).

For  $N=2$ , there are three excitons which have very close energies and all of them also have a significant interband dipole. Using an optical excitation which excites all three excitons (excitons 2, 3, and 4) results in a superposition of these three transitions [Fig. 4(a)]. Therefore for a low temperature calculation ( $T=50$  K) [Fig. 4(b)] the modulations of the optical fluorescence show a complicated pattern determined by the three relevant energy differences.

### B. Coherent terahertz emission

The coherent signal is calculated using Eq. (3.2). Since our basis set is localized in real space, intraband dipoles are assumed to be diagonal in the quantum-well index

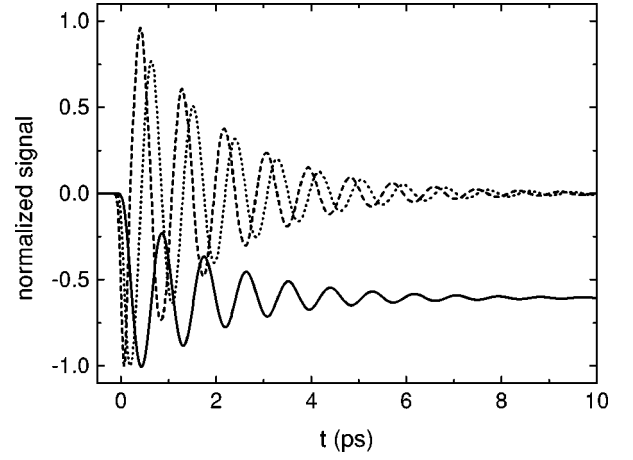


FIG. 5. Normalized intraband-polarization (solid line), derivative of that which is proportional to the current  $j$  (dotted line), and second derivative of that which is proportional to the emitted (far-field) THz field (dashed line).  $N=2$ ,  $eFd=10$  meV,  $T=300$  K.

$$M_{mn}^{ee} = -\delta_{mn}e(m-N/2)d, \quad M_{mn}^{hh} = \delta_{mn}e(m-N/2)d. \quad (5.11)$$

The  $N/2$  term arises in the definition of the intraband dipoles, since the origin of the coordinate system corresponds to the middle of the nanostructure. Using a different origin would modify the value of the intraband polarization, but would have no effect on its time derivatives which determine the current and the THz signal. Substituting Eq. (5.11) into Eq. (2.20), we obtain

$$P_b = \sum_n (\mu_n^e c_n^\dagger c_n + \mu_n^h d_n^\dagger d_n), \quad (5.12)$$

with  $\mu_n^e = -\mu_n^h = -e(n-N/2)d$ . The coherent signal can then be expressed into an alternative form

$$S^{(c)}(t) \propto \frac{\partial^2}{\partial t^2} \sum_n [\mu_n^e \rho_n^e(t) + \mu_n^h \rho_n^h(t)], \quad (5.13)$$

where  $\rho_n^e$  and  $\rho_n^h$  are the real space electron and hole probability density of  $n$ 'th quantum well and can be calculated using the exciton doorway function  $N_{\alpha\beta}$  as

$$\rho_m^e(t) = \sum_{nn',\alpha\beta} \Psi_{mn,\alpha}^* \Psi_{mn',\beta} N_{\alpha\beta}(t), \quad (5.14)$$

$$\rho_n^h(t) = \sum_{mm',\alpha\beta} \Psi_{mn,\alpha}^* \Psi_{m'n,\beta} N_{\alpha\beta}(t). \quad (5.15)$$

Figure 5 shows the THz signal using the same parameters as in Fig. 2(b). The optical excitation in the presence of the applied field leads to the excitation of polarized excitons (i.e., where electrons and holes are not at the same position in space).<sup>31</sup> This instantaneous contribution to the intraband polarization is reflected by the fast creation of the intraband polarization which follows the excitation pulse.<sup>6,31,39</sup> At later times the intraband polarization oscillates with a frequency corresponding to energy differences between the dressed excited excitonic states. The current associated with the motion of the excited wave packet is given by the time derivative of the intraband polarization. The emitted far field, which can

be observed experimentally, is the second derivative with respect to time of the intraband polarization.

In the exciton representation the rapid modulations of the THz signal are determined by off-diagonal components of  $N_{\alpha\beta}$ . For the parameters used in Fig. 5, there are only three relevant excitons and coherences between them, which are optically excited and may contribute to the THz signal (see Fig. 3). The coherent THz radiation depends on the product of exciton coherences with the off-diagonal components of the intraband dipole matrix. Since there is a significant intraband dipole only between the highest and the lowest of the three excited excitons (exciton 2 and 4), the coherence between these excitons gives by far the strongest contribution to the intraband emission. The intraband dipoles between excitons 2 to 3 and 3 to 4 are very weak and their contribution to the THz signal are very small. The decay of the modulations in the coherent THz signal is determined by the phonon-induced decay of the coherence between the excitons [see Fig. 3(d)]. Therefore, in the exciton representation, the modulations of the THz signal are due to a coherent superposition of the same exciton states as in the fluorescence. However, these two signals may show different behavior, since they differ in the window function, which is determined by the interband and intraband dipoles, respectively. Only the fast frequency ( $E_2 - E_4$ ) that is present in the fluorescence also shows up in the intraband polarization and consequently in the THz signal, see Fig. 4(b) and Fig. 5. In the long time limit (which is not reached by the few ps covered by our time-domain calculations) after all the coherences have decayed, the system of phonon-dressed excitons will eventually reach a thermal equilibrium.

Figure 6 shows the combined effects of phonons and disorder on THz emission. Figure 6(a) illustrates the increase of the phonon-induced dephasing of the THz-signal as the temperature is raised (without disorder). Shown are calculations for  $T=50$  K (dash-dot-dot line),  $T=100$  K (short-dash line), and  $T=300$  K (dotted line). Compared to the frequency of the THz signal for the present parameters the frequency shift induced by the phonons is small, and there is almost no frequency change of the modulations with increasing temperature. Figure 6(b) shows the THz signal without phonon and disorder (dash-dot line), disorder alone (dashed line), and both phonon and disorder (solid line). At low temperatures the disorder results in a dephasing of the THz signal.<sup>27</sup> At higher temperatures (for the present parameters) the phonon-induced dephasing is stronger than the dephasing induced by the disorder. This was already discussed using Fig. 2.

Figure 7 displays the effect of system size on the THz signal. Shown in (a) is the influence of the disorder alone for  $N=2$  (solid line) and  $N=3$  (dashed line) using  $eFd = 10$  meV. The normalized amplitude (i.e., divided by the number of wells  $N$ ) of the signal for short times comparing  $N=2$  and  $N=3$  is not very different, but it is clear to see that the dephasing rate of the signal increases with increasing size. This may be explained as follows: whereas the phonons couple more or less in the same way to the different optically excited excitons, disorder affects them for each realization in a different way. This is due to the fact that the excitons are extended over a few wells (otherwise there would be no modulation of the intraband polarization) and the disorder

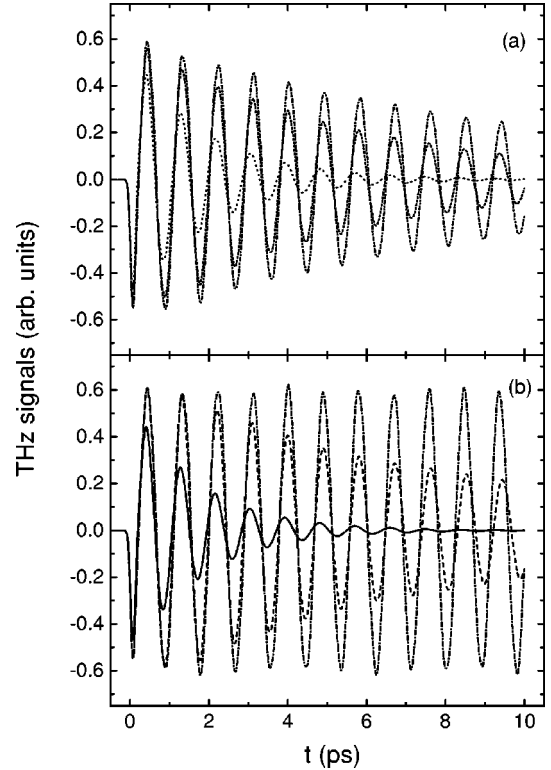


FIG. 6. THz signals for  $N=2$ ,  $eFd=10$  meV. (a) dash-dot-dot line: with phonons at  $T=50$  K, short-dashed line:  $T=100$  K, dotted line:  $T=300$  K; (b) dash-dot line: without phonons and disorder, dashed line: disorder only, solid line: with both phonons ( $T=300$  K) and disorder.

between different wells is taken to be uncorrelated. Figure 7(b) shows the normalized THz-signal with phonons at  $T=300$  K, and  $eFd=10$  meV (without disorder). Shown are for  $N=2$  (solid line),  $N=3$  (dashed line),  $N=4$  (dotted line), and  $N=5$  (dash-dotted line). We see that the signal increases slightly with the size and that the dephasing as well as the frequency remains basically unchanged. This indicates that for the present parameters (large field  $eFd=10$  meV and large Coulomb-interaction  $9$  meV, compared to weak interwell coupling  $2.25$  meV +  $0.25$  meV =  $2.5$  meV) the excitons are quite localized, i.e., the wave function amplitude is rather strong in a few quantum wells.

Figure 8 displays the time- and frequency-resolved incoherent THz signal for  $N=2$ ,  $eFd=10$  meV,  $T=300$  K. A similar modulation shows up as in the time-domain coherent THz signal. For long times the incoherent signal, which is defined as a polarization-polarization correlation function, attains a finite long time value, since the intraband polarization approaches a constant long time value, see Fig. 5. It also shows the frequency resonances between exciton 2 and 4. (a) and (b) give the plots of frequency- and time-resolved incoherent THz signal, where (a) displays the frequency-resolved signal for a fixed time of  $t=0.55$  ps and (b) is for the time-resolved signal for a fixed frequency of  $\omega=0.6$  meV.

In real space, the origin of the THz signal is simply the motion of the charges, i.e., electrons and holes, see Eq. (5.13). This charge oscillation is displayed in Fig. 9, where the electron and hole populations in the different quantum wells are shown. (a) and (b) displays the electron and hole

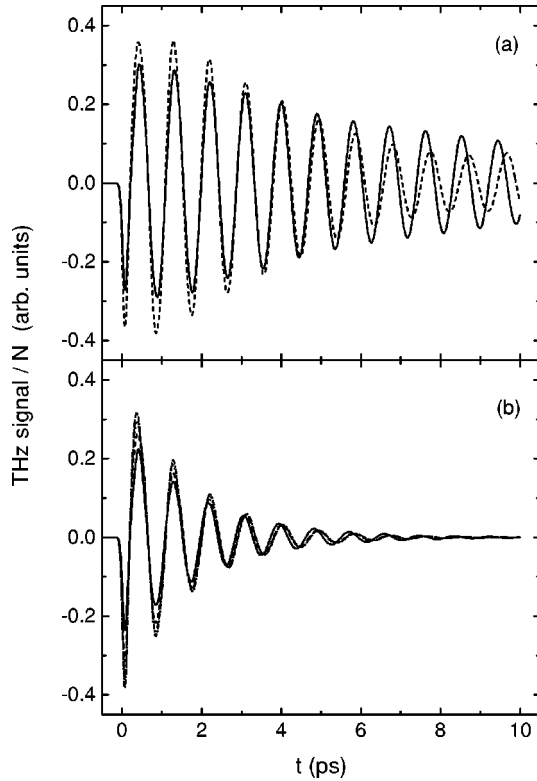


FIG. 7. (a) THz signals (without phonons, with disorder) divided by number of quantum wells  $N$  for  $N=2$  (solid) and 3 (dashed line). (b) THz signals (with phonons at  $T=300$  K, and without disorder) divided by number of quantum wells  $N$  for  $N=2$  (solid), 3 (dashed), 4 (dotted), and 5 (dash-dotted).

populations for  $N=2$ , respectively. (c) and (d) are for  $N=5$ . One can see that electrons are mainly responsible for the charge oscillations between the quantum wells. Due to their larger mass, the hole populations show only very weak modulations. The time-period of the modulations of the population shown in Fig. 9 is determined by the energy difference between the two excitons that contribute strongly to the intraband polarization. In the long time limit the phonon-induced relaxation may lead to a charge separation between electrons and holes. It can be seen in Fig. 9 that there is a tendency that electrons and holes move (*relax*) towards different end of the nanostructure in real space.

## VI. SUMMARY

In this paper we have calculated the intraband emission resulting from the second-order polarization induced by a femtosecond pump field using an exciton model for coupled semiconductor quantum wells. Exciton-phonon coupling represented by arbitrary spectral densities has been incorporated into the equations of motion for exciton polarizations, as well as exciton populations and coherences through Redfield's theory. Applications to a simple one-dimensional model for coupled semiconductor quantum wells with an applied external electric field demonstrate the interplay of coherent THz and incoherent fluorescence radiation. The relative strength of bound exciton versus continuum contributions, as well as the Coulombic effects, in general are overestimated in a one-dimensional model.<sup>22</sup> Extensions of this approach to three-dimensional descriptions would be

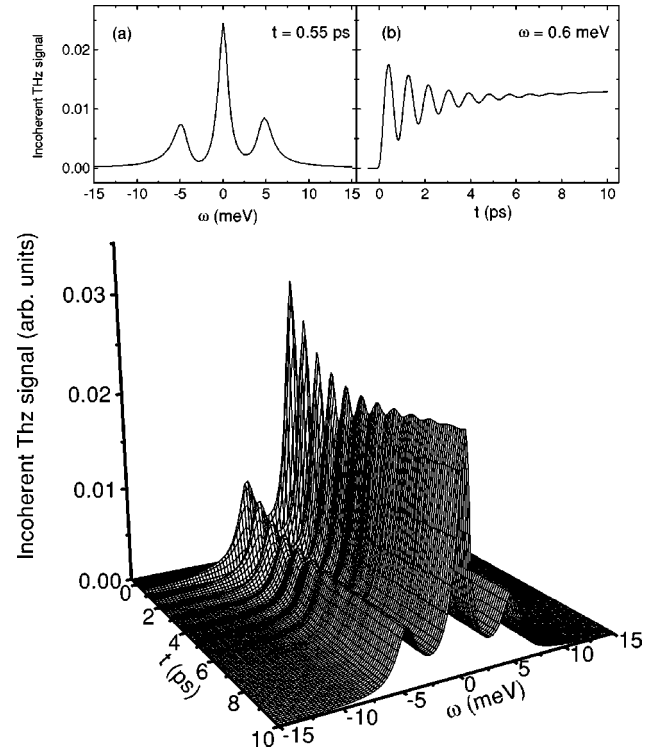


FIG. 8. Three-dimensional plot of time- and frequency-resolved incoherent THz signal for  $N=2$ ,  $eFd=10$  meV. (a) frequency-resolved plot for  $t=0.55$  ps, (b) time-resolved plot for  $\omega=0.6$  meV.

highly desirable and can be expected to give new insight into the interplay between coherent and incoherent dynamics which strongly affects experimentally observed THz emission.<sup>4,5,26</sup> Full three-dimensional calculations<sup>8,14,22</sup> require a considerably larger numerical effort in calculating the exciton states. A doorway-window picture<sup>28</sup> based on the reduced single-electron density matrix is developed for the analysis of these signals. Within our approach the coherent and the incoherent THz signals as well as the optical fluorescence oscillate with frequencies determined by the differences between the energies of phonon-dressed excitons. The damping of the coherent oscillations due to phonon-induced relaxation between different exciton states has been demonstrated. The approach presented here can describe the phonon-induced transition starting with coherent (oscillating) carrier motion to charge separation (real transport), using the excitonic eigenstates of the system.

## ACKNOWLEDGMENTS

The support of the Air Force Office of Scientific Research through Grant No. AFOSR-95-F49620-96-1-0030, and the National Science Foundation through Grants No. CHE-9526125 and No. PHY94-15583, is gratefully acknowledged.

## APPENDIX: THE RELAXATION SUPEROPERATORS

All relevant information with regard to phonon dynamics is contained in the matrix of spectral densities  $C_{mn,kl}^{ij}(\omega)$ ,<sup>28</sup> where the superscripts  $i$  and  $j$  assume the values  $e$  and  $h$ :

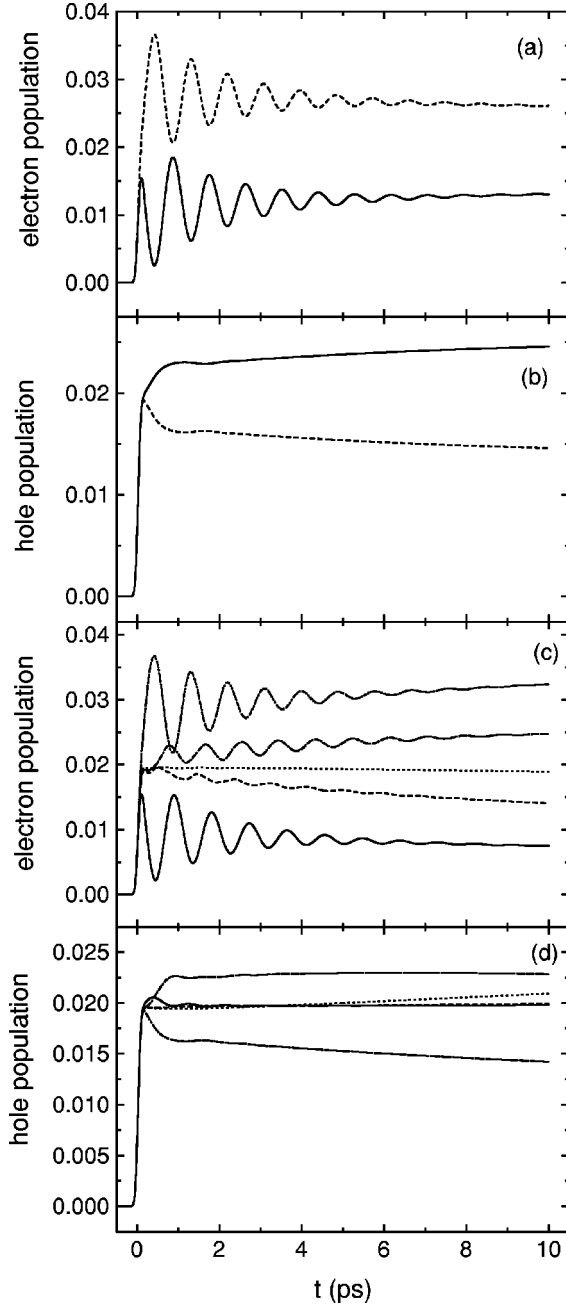


FIG. 9. Real space electron and hole populations. (a) and (b) are for  $N=2$ . (a) solid line:  $\rho_1^e$ , dashed line:  $\rho_2^e$ ; (b) solid line:  $\rho_1^h$ , dashed line:  $\rho_2^h$ . (c) and (d) are for  $N=5$ . (c) solid line:  $\rho_1^e$ , dashed line:  $\rho_2^e$ , dotted line:  $\rho_3^e$ , dash-dotted line:  $\rho_4^e$ , dash-dot-dotted line:  $\rho_5^e$ ; (d) solid line:  $\rho_1^h$ , dashed line:  $\rho_2^h$ , dotted line:  $\rho_3^h$ , dash-dotted line:  $\rho_4^h$ , dash-dot-dotted line:  $\rho_5^h$ .

$$C_{mn,kl}^{ij}(\omega) \equiv \sum_s \frac{m_s \omega_s^3}{4} z_{mn,s}^i z_{kl,s}^j 2\pi [\delta(\omega - \omega_s) - \delta(\omega + \omega_s)]. \quad (\text{A1})$$

Equation (A1) applies for a harmonic bath linearly coupled to intraband components of the density matrix operator in the most general way. The index  $s$  represents the bath oscillators with frequency  $\omega_s$ . The matrix of spectral densities in Eq. (A1) is a straightforward generalization of the spectral density<sup>28,40</sup> to the case when each bath oscillator is coupled to several electronic transitions. Matrices of spectral den-

sities have been introduced in Ref. 41 and applied in Refs. 32 and 42 to Frenkel exciton models.

In the exciton representation, the matrix of spectral densities  $C_{\alpha\beta,\mu\nu}(\omega)$  assumes the form<sup>42</sup>

$$C_{\alpha\beta,\mu\nu}(\omega) \equiv \sum_s \frac{m_s \omega_s^3}{4} \mathcal{D}_{\alpha\beta,s} \mathcal{D}_{\mu\nu,s} 2\pi [\delta(\omega - \omega_s) - \delta(\omega + \omega_s)]. \quad (\text{A2})$$

This gives

$$C_{\alpha\beta,\mu\nu}(\omega) = \sum_{m n k l} \sum_{m' n' k' l'} [C_{mn,kl}^{ee}(\omega) \delta_{m'n'} \delta_{k'l'} + C_{mn,k'l'}^{eh}(\omega) \delta_{m'n'} \delta_{kl} + C_{m'n',kl}^{he}(\omega) \delta_{mn} \delta_{k'l'} + C_{m'n',k'l'}^{hh}(\omega) \delta_{mn} \delta_{kl}] \Psi_{mm',\alpha}^* \times \Psi_{nn',\beta} \Psi_{kk',\mu}^* \Psi_{ll',\nu}. \quad (\text{A3})$$

The relaxation superoperators appearing in Eqs. (2.21) and (2.22) are derived in Ref. 29 and have the form

$$\Gamma_{\mu\nu} = \sum_{\alpha\beta\nu'} \int_0^\infty dt G_{\alpha\beta}(t) G_{\nu',\nu}^*(t) U_{\mu\alpha,\beta\nu'}(t), \quad (\text{A4})$$

$$R_{\mu\nu,\mu'\nu'} = \sum_{\alpha\beta\alpha'\beta'} \int_0^\infty dt [G_{\mu\alpha}^*(t) G_{\alpha\mu'}(t) G_{\alpha'\beta'}(t) \times G_{\beta\nu'}^*(t) U_{\nu\alpha',\beta'\beta}(t) + G_{\nu\alpha}(t) G_{\alpha\nu'}^*(t) G_{\alpha'\beta'}(t) \times G_{\beta\mu'}(t) U_{\mu\alpha',\beta'\beta}(-t) - G_{\alpha'\alpha}(t) \times G_{\alpha\mu'}(t) G_{\nu\beta'}(t) G_{\beta\nu'}^*(t) U_{\mu\alpha',\beta'\beta}(t) - G_{\alpha'\alpha}(t) G_{\alpha\nu'}^*(t) G_{\mu\beta'}(t) \times G_{\beta\mu'}(t) U_{\nu\alpha',\beta'\beta}(-t)], \quad (\text{A5})$$

where  $U_{\mu\nu,\alpha\beta}(t)$  is the phonon Greens function<sup>29</sup> expressed in terms of spectral densities:

$$U_{\mu\nu,\alpha\beta}(t) = \int_{-\infty}^{\infty} \frac{d\omega}{2\pi} C_{\mu\nu,\alpha\beta}(\omega) \left[ \coth\left(\frac{\hbar\omega}{2kT}\right) \cos(\omega t) - i \sin(\omega t) \right], \quad (\text{A6})$$

$T$  is the temperature, and  $G$  is the one exciton Green of Eq. (2.21) with  $h_{\mu\nu}^{(1)} = \delta_{\mu\nu} \epsilon_\mu$ , which is diagonal in the exciton basis  $G_{\mu\nu}(t) = \delta_{\mu\nu} \exp(-i\epsilon_\mu t)$ . This yields

$$\Gamma_{\mu\nu} = \sum_\alpha \int_0^\infty dt \exp[-i(\epsilon_\alpha - \epsilon_\nu)t] U_{\mu\alpha,\alpha\nu}(t), \quad (\text{A7})$$

$$R_{\mu\nu,\mu'\nu'} = \sum_\alpha \int_0^\infty dt [\exp[-i(\epsilon_\alpha - \epsilon_{\nu'})t] U_{\nu\alpha,\alpha\nu'}(t) \delta_{\mu\mu'} + \exp[i(\epsilon_\alpha - \epsilon_{\mu'})t] U_{\mu\alpha,\alpha\mu'}(-t) \delta_{\nu\nu'} - \exp[-i(\epsilon_{\nu'} - \epsilon_{\nu'})t] U_{\mu\mu',\nu\nu'}(t) - \exp[i(\epsilon_\mu - \epsilon_{\mu'})t] U_{\nu\nu',\mu\mu'}(-t)]. \quad (\text{A8})$$

- \*Present address: Department of Physics and Material Sciences Center, Philipps University, Renthof 5, D-35032 Marburg, Germany. Electronic address: torsten.meier@physik.uni-marburg.de
- <sup>1</sup>B.B. Hu, X.C. Zhang, and D.H. Auston, *Phys. Rev. Lett.* **67**, 2709 (1991).
  - <sup>2</sup>X.-C. Zhang and D.H. Auston, *Appl. Phys. Lett.* **59**, 768 (1991).
  - <sup>3</sup>P.C.M. Planken, M.C. Nuss, I. Brener, K.W. Goossen, M.S.C. Luo, S.L. Chuang, and L. Pfeiffer, *Phys. Rev. Lett.* **69**, 3800 (1992).
  - <sup>4</sup>H.G. Roskos, M.C. Nuss, J. Shah, K. Leo, D.A.B. Miller, A.M. Fox, S. Schmitt-Rink, and K. Köhler, *Phys. Rev. Lett.* **68**, 2216 (1992).
  - <sup>5</sup>C. Waschke, H.G. Roskos, R. Schwedler, K. Leo, H. Kurz, and K. Köhler, *Phys. Rev. Lett.* **70**, 3319 (1993).
  - <sup>6</sup>E. Binder, T. Kuhn, and G. Mahler, *Phys. Rev. B* **50**, 18 319 (1994).
  - <sup>7</sup>C. Chansungsan, L. Tsang, and S.L. Chuang, *J. Opt. Soc. Am. B* **11**, 2508 (1995).
  - <sup>8</sup>T. Meier, F. Rossi, P. Thomas, and S.W. Koch, *Phys. Rev. Lett.* **75**, 2558 (1995).
  - <sup>9</sup>W. Huhn and A. Stahl, *Phys. Status Solidi B* **124**, 167 (1984); S. Schmitt-Rink, D.S. Chemla, and H. Haug, *Phys. Rev. B* **37**, 941 (1988); M. Lindberg and S.W. Koch, *ibid.* **38**, 3342 (1988).
  - <sup>10</sup>For a textbook discussion of the semiconductor Bloch equations see H. Haug and S.W. Koch, *Quantum Theory of the Optical and Electronic Properties of Semiconductors*, 3rd ed. (World Scientific, Singapore, 1994).
  - <sup>11</sup>Y.Z. Hu, R. Binder, and S.W. Koch, *Phys. Rev. B* **47**, 15 679 (1993).
  - <sup>12</sup>I.E. Perakis, *Chem. Phys.* **210**, 259 (1996).
  - <sup>13</sup>E. Binder, D. Preißer, and T. Kuhn, *Proceedings of the ESSOERC 1996*, edited by G. Baccarani and M. Rudan (Editions Frontières, Paris, 1996), p. 549.
  - <sup>14</sup>T. Meier, P. Thomas, and S.W. Koch, *Phys. Low-Dimens. Semicond. Struct.* **3/4**, 1 (1998); T. Meier, P. Thomas, and S. W. Koch, *Ultrafast Phenomena in Semiconductors*, edited by K. T. Tsen (Springer, New York, in press).
  - <sup>15</sup>S. Haas, F. Rossi, and T. Kuhn, *Phys. Rev. B* **53**, 12 855 (1996).
  - <sup>16</sup>J. Hader, T. Meier, S.W. Koch, F. Rossi, and N. Linder, *Phys. Rev. B* **55**, 13 799 (1997).
  - <sup>17</sup>E. Binder and T. Kuhn, *Hot Carrier in Semiconductors*, edited by K. Hess, J.-P. Leburton, and U. Ravaioli (Plenum Press, New York, 1996), p. 213.
  - <sup>18</sup>F. Rossi, M. Gulia, P.E. Selbmann, E. Molinari, T. Meier, P. Thomas, and S.W. Koch, in *The Physics of Semiconductors, Proceedings of the 23rd ICPS*, edited by M. Scheffler and R. Zimmermann (World Scientific, Singapore, 1996), p. 1775.
  - <sup>19</sup>R. Brunetti, C. Jacoboni, and F. Rossi, *Phys. Rev. B* **39**, 10 781 (1989).
  - <sup>20</sup>M.M. Dignam and J.E. Sipe, *Phys. Rev. Lett.* **64**, 1797 (1990); *Phys. Rev. B* **43**, 4097 (1991).
  - <sup>21</sup>M.M. Dignam, J. Shah, and J.E. Sipe, *Phys. Rev. B* **49**, 10 502 (1994).
  - <sup>22</sup>J. Hader, P. Thomas, and S.W. Koch, *Prog. Quantum Electron.* **22**, 123 (1998).
  - <sup>23</sup>T. Meier, G. von Plessen, P. Thomas, and S.W. Koch, *Phys. Rev. B* **51**, 14 490 (1995).
  - <sup>24</sup>T. Meier, G. von Plessen, P. Thomas, and S.W. Koch, *Phys. Rev. Lett.* **73**, 902 (1994).
  - <sup>25</sup>V.M. Axt, G. Bartels, and A. Stahl, *Phys. Rev. Lett.* **76**, 2543 (1996).
  - <sup>26</sup>P. Haring Bolivar, F. Wolter, A. Müller, H.G. Roskos, H. Kurz, and K. Köhler, *Phys. Rev. Lett.* **78**, 2232 (1997).
  - <sup>27</sup>J.P. Reynolds and M. Luban, *Phys. Rev. B* **54**, 14 301 (1996).
  - <sup>28</sup>S. Mukamel, *Principles of Nonlinear Optical Spectroscopy* (Oxford University Press, New York, 1995).
  - <sup>29</sup>V. Chernyak, W.M. Zhang, and S. Mukamel, *J. Chem. Phys.* **109**, 9587 (1998).
  - <sup>30</sup>V. Chernyak and S. Mukamel, *J. Opt. Soc. Am. B* **13**, 1302 (1996).
  - <sup>31</sup>S.L. Chuang, S. Schmitt-Rink, B.I. Greene, P.N. Saeta, and A.F.J. Levi, *Phys. Rev. Lett.* **68**, 102 (1992).
  - <sup>32</sup>W.M. Zhang, T. Meier, V. Chernyak, and S. Mukamel, *J. Chem. Phys.* **108**, 7763 (1998); *Proc. R. Soc. London, Ser. A* **356**, 405 (1998).
  - <sup>33</sup>V. Chernyak and S. Mukamel, in *Notions and Perspectives of Nonlinear Optics*, edited by O. Keller (World Scientific, Singapore, 1996), Vol. 3, pp. 93–120.
  - <sup>34</sup>P. Kner, S. Bad-Ad, M.V. Marquezini, D.S. Chemla, and W. Schäfer, *Phys. Rev. Lett.* **78**, 1319 (1997); P. Kner, W. Schäfer, R. Lövenich, and D.S. Chemla, *ibid.* **81**, 5386 (1998).
  - <sup>35</sup>G. von Plessen, T. Meier, M. Koch, J. Feldmann, P. Thomas, S.W. Koch, E.O. Göbel, K.W. Goosen, J.M. Kuo, and R.F. Kopf, *Phys. Rev. B* **53**, 13 688 (1996).
  - <sup>36</sup>A.M. Fox, D.A.B. Miller, J.E. Cunningham, W.Y. Yan, C.Y.P. Chao, and S.L. Chuang, *Phys. Rev. B* **46**, 15 365 (1992).
  - <sup>37</sup>T. Stroucken, A. Knorr, P. Thomas, and S.W. Koch, *Phys. Rev. B* **53**, 2026 (1996).
  - <sup>38</sup>The proper inclusion of the energetic disorder requires that similar calculations are repeated a lot of times for different realization of the disorder until the resulting signals are converged. Typically we had to use 1000 to 2000 realization to get convergence. Due to this increase in the numerical effort the calculations with disorder were only performed for  $N=2$  and 3.
  - <sup>39</sup>P.C.M. Planken, M.C. Nuss, W.H. Knox, D.A.B. Miller, and K.W. Goossen, *Appl. Phys. Lett.* **61**, 2009 (1992).
  - <sup>40</sup>U. Weiss, *Quantum Dissipative Systems* (World Scientific, Singapore, 1993).
  - <sup>41</sup>V. Chernyak and S. Mukamel, *J. Chem. Phys.* **105**, 4565 (1996).
  - <sup>42</sup>T. Meier, V. Chernyak, and S. Mukamel, *J. Chem. Phys.* **107**, 8759 (1997).